Bull Volcanol (2001) 63:191–203
DOI 10.1007/s004450100135

RESEARCH ARTICLE

Thomas R. Walter · Valentin R. Troll

Formation of caldera periphery faults: an experimental study

Received: 19 September 2000 / Accepted: 12 February 2001 / Published online: 4 May 2001

Abstract Changing stresses in multi-stage caldera volcanoes were simulated in scaled analogue experiments aiming to reconstruct the mechanism(s) associated with caldera formation and the corresponding zones of structural weakness. We evaluate characteristic structures resulting from doming (chamber inflation), evacuation collapse (chamber deflation) and cyclic resurgence (inflation and deflation), and we analyse the consequential fault patterns and their statistical relationship to morphology and geometry. Doming results in radial fractures and subordinate concentric reverse faults which propagate divergently from the chamber upwards with increasing dilation. The structural dome so produced is characterised by steepening in the periphery, whereas the broadening apex subsides. Pure evacuation causes the chamber roof to collapse along adjacent bell-shaped reverse faults. The distribution of concentric faults is influenced by the initial edifice morphology; steep and irregular initial flanks result in a tilted or chaotic caldera floor. The third set of experiments focused on the structural interaction of cyclic inflation and subsequent moderate deflation. Following doming, caldera subsidence produces concentric faults that characteristically crosscut radial cracks of the dome. The flanks of the edifice relax, resulting in discontinuous circumferential faults that outline a structural network of radial and concentric faults; the latter form locally uplifted and tilted wedges (half-grabens) that grade into horst-and-graben structures. This superimposed fault pattern also extends inside the caldera. We suggest that major pressure deviations in magma chamber(s) are reflected in the fault arrangement dissecting the volcano flanks and may be used as a first-order indication of the processes and mechanisms involved in caldera formation.

Keywords Multi-stage caldera volcanoes · Caldera periphery faults · Volcano fractures · Flank instability

Editorial responsibility: T.H. Druitt

T.R. Walter (✉) · V.R. Troll
Abteilung Vulkanologie und Petrologie,
GEOMAR Forschungszentrum, Wischhofstrasse 1–3, 24148 Kiel, Germany
e-mail: twalter@geomar.de
Tel.: +49-431-6002652, Fax: +49-431-6001400

Introduction

Large, multi-stage "ash-flow calderas" are thought to form mainly during voluminous ignimbrite eruptions (e.g. Smith and Bailey 1968; Schmincke 1969; Williams and McBirney 1979; Druitt and Sparks 1984; Newhall and Dzurisin 1988; Lipman 1997). Rapid decompression of a shallow magma chamber during large eruptions causes deflation and the chamber roof subsides into the "void" thus created (Smith and Bailey 1968; Druitt and Sparks 1984). In addition to extensive field studies of caldera volcanoes (see Lipman 1997, and references therein), caldera formation has been studied theoretically and experimentally (Wisser 1927; Prucha 1965; Komuro et al. 1984; Komuro 1987; Gudmundsson 1988; Marti et al. 1994; Branney 1995; Gudmundsson et al. 1997; Odonne et al. 1999; Roche et al. 2000; Marti et al. 2000). Caldera volcanoes illustrate structural elements of several types, with arrangements and quantities depending on, for example, the physical properties of the country rocks, pre-existing tectonic structures or a regional stress field, the geometry and dynamics of the magma chamber and the volcanic load. Inflation of a magma chamber causes volumetric spreading and swelling, combined with the effect of hundreds to thousands of intrusions, distributed mainly in radial or circumferential order (Komuro et al. 1984; Walker 1999). Also, radial and circumferential fractures develop in scaled experiments by inflation of an analogue reservoir (e.g. Marti et al. 1994), which contrasts with the exclusively concentric structures of pure evacuation collapse (Komuro 1987; Roche et al. 2000). Caldera volcanoes with several episodes of chamber inflation and evacuation collapse are thus likely to produce intersecting structural systems (Komuro 1987; Marti et

al. 1994). The inflation of a chamber as a result of pressure increase (e.g. due to replenishment) is detected by uplift of the ground surface, accompanied by magma chamber wall burst and dyke growth (McLeod and Tait 1999). Tilt measurements on active volcanoes show that they undergo repeated inflation and deflation. Volcano inflation is slow, whereas deflation is very rapid, but the amounts of inflation and deflation are generally very similar (Swanson 1982).

Moreover, complex caldera periphery dykes and faults are common andsurround caldera volcanoes on earth (Smith and Bailey 1968) and other planets (Thomas et al. 1990). The formation of this peripheral system, however, has received little attention in the literature and remains poorly understood. Since intracaldera structural relations are normally hidden, the extracaldera periphery fault system may help to reconstruct the evolution of such calderas in the field.

To better understand peripheral caldera faults and their relations to magma chamber dynamics, we experimentally studied the overall caldera fracture system for the cases of (a) pure doming, (b) pure evacuation collapse and (c) the combination of both. Herein, we focus on the geometry and propagation of the fractures produced by these scenarios and their relationship to chamber depth, chamber size, material properties and edifice morphology. We refer to natural examples where the arrangement of faults and dykes indicates the mechanism(s) from which those patterns originate.

Experimental set-up

Inflatable reservoirs were constructed by attaching two equivalent-sized mats of very thin stretchy rubber at the outer rims. In the lower mat, we inserted an inlet and connected a pipe system, through which inflation and evacuation of a balloon was accomplished. An outflow valve was joined to the pipe. The volume of air/water within the balloon–pipe system was held constant for various initial geometric parameters. The balloon(s) were sill-like in shape with radii ranging from 6 to 12 cm and were inflated up to a height of 6 cm. To test the influence of the shape of the reservoir, experiments were also carried out using oval-shaped balloons.

A glass tank with the dimension of approximately 1 m^3 was filled to a depth of several tens of centimetres with granular analogue material. The balloon was placed in the centre of the box and a mound was constructed above, so as to simulate a volcanic cone (Fig. 1).

In separate set-ups, we varied the shape and size of the reservoir and the cone, in order to evaluate the relevance of individual geometric parameters for the models. More than 30 different geometries defined by these parameters were examined.

Analogue models were geometrically scaled to fit natural ocean-island volcanoes (cf. Schmincke 1976; Ye et al. 1999), where regional tectonic influences are believed to be small. The general set-up of the experiments simulated sill-like shallow magma chambers situated at depths between 5 and 15 km below the surface of a volcanic edifice. The geometric scaling factor was 10^{-5}, so that 1 cm in the experiment is approximately equivalent to 1 km in nature. The geometric similarity of the models is based on the ratios of the external forces, gravity forces, internal friction forces and resistant forces against failure. Experimental scaling followed Hubbert (1937), Sanford (1959) and Komuro et al. (1984), using the suggested ratios of external forces to gravity force and of internal friction to resistant forces. The generality and relation ofthe experimentally derived fault sites was established by using two analogue materials, medium-grained sand and wheat flour. Both analogue materials were measured mechanically in direct shear tests. Dry medium-grained sand is characterised by low cohesionand obeys the Mohr-Coulomb failure criterion (cf. Hubbert 1951; Byerlee 1978; Mandl 1988) with scaled yield strength and internal friction angles (ϕ) resembling those of volcanic rocks (e.g. for basalt ϕ_B=30–45°).

Sand has been widely used as a modelling material (Hubbert 1937, 1951; Sanford 1959; Ramberg 1981); its mechanical properties are well known (see Cobbold and Castro 1999 for review). We used sieved quartz sand with a mean diameter of 500 µm mixed with a subordinate amount of clay minerals, a bulk density of 1.5–1.7 g cm^{-3} (depending on consolidation) and a coefficient of internal friction (μ) of μ_s=0.6 (i.e. ϕ_S=31°). The cohesion (C) of sand was controlled by the pore-water pressure, and determined in direct shear tests and undrained triaxial tests. The natural cohesion is in the range of 10^5–10^7 Pa (e.g. Hoshino et al. 1972; Glicken et al. 1980). Higher standards of 10^7 Pa represent values of small laboratory samples, whereas 10^6 Pa approaches the cohesion lowered by large-scale inhomogeneity effects (Schultz 1996). An analogue material with an average mean cohesion scaling to ca. 5×10^6 Pa was therefore

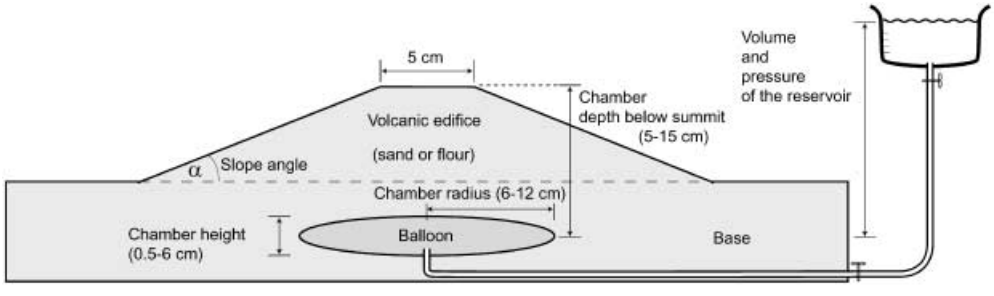

Fig. 1 Experimental set-up: the geometry was systematically changed for slope angle, cone height, chamber depth below the summit and the chamber size (height, width). See text for details

chosen to be appropriate. The pore-water pressure in sand was accordingly held at a value so that the cohesion was approximately 5×10^1 Pa (C_S=40–50 Pa). Once dilated, the cohesion of sand decreases and allows fault reactivation (Krantz 1991). Elastic strain, however, cannot be studied in sand models (Cobbold and Castro 1999).

The second analogue material was dry flour (grain size 100–200 μm). Its mechanical properties were found to be complementary to medium-grained sand in being more cohesive (C_F=35 Pa) relative to its density (~0.57 g cm^{-3}). Dry flour, therefore, deforms little under its own weight and offers the possibility to study the geometry and propagation of faults in detail; tensional strength was not to scale. The coefficient of internal friction for flour is μ_F=0.65 (ϕ_F=33°).

Edge effects were kept at a minimum by using a very big glass tank and a highly elastic and thin balloon material, where the finite size of the balloon allowed control of its deformation. On the other hand, however, to deform the elastic walls of the balloon during inflation, its internal pressure needed to be high relative to the load (i.e. lithostatic pressure). As a result, the balloons entail the deformation of the roof, not the contrary. Eruptions during high magma-chamber pressures could not form, so that the wide range of modelled doming discussed here possibly includes some structural end members, not observed in nature.

We used three methods to obtain and compare three-dimensional data on the orientation and propagation of faults:

1. The depth of the balloon was systematically changed within a set of models of the same morphology.
2 Models were saturated in water and sectioned after deformation.
3. A set of experiments was performed against a transparent glass pane.

The surfacedeformation was filmed and photographed and the length, distance and displacement of each fault type was measured and recorded (Table 1). The positions of the observed circumferential (concentric) faults are described as a function of the volcano perimeter and the total distances from the centre.

Results

The results are summarised according to the three end-member mechanisms of pure doming (reservoir inflation), pure evacuation collapse (reservoir deflation), and recurring inflation and deflation. For each of those mechanisms, we checked the influence of the initial volcano morphology and gravitational forces. Additionally, the influence of different chamber depths was tested for each of these set-ups. Every experiment was reproduced and performed for both analogue materials.

Pure doming

A plateau surface was arranged in separate experimental set-ups at 5, 7, 9, 11, 13 and 15 cm above the balloon. Upon balloon inflation, the surface fractured forming radial cracks that propagated outwards from a central polygonal block (Fig. 2). The radial fractures propagated perpendicularly to the least principal compressive stress σ_3 and parallel to the maximum principal compressive stress σ_1, with displacements approximately normal to the fracture surface (mode-I fractures). Independent of the experimental geometries and analogue material, concentric reverse (thrust) faults formed sub-perpendicular to the opening radial cracks, resulting in a morphological "s-shaped" flank deformation (Fig. 2). The dip of these curved concentric faults decreased towards the periphery and within individual set-ups as a function of increasing chamber depth. The relative motion of the fracture combined extensional and shear displacements, propagating upwards. The uplifted flanks also produced a flattening and subsequent polygonal apical graben structure (i.e. proto-caldera) in all doming experiments, similar to those described by Komuro (1987) and Marti et al. (1994). The apical graben was chiefly limited by steep, rotational normal faults. The depression widened by polygonal blocks that were detached from the oversteepened walls. Some apical grabens were defined by only one tilted and/or downward slumped angular block.

Experiments with deeper balloons resulted in larger areas of (a) tumescence, (b) apical graben and (c) radial cracks. Deeper situated reservoirs resulted moreover in a reduced domal uplift and a reduced apical graben subsidence.

For cone-shaped morphologies, doming produced a more heterogeneous radial fault pattern compared with the plateau-shaped morphology. This is most likely a function of the model construction, differing slightly from an ideally shaped cone.

Greater initial flank inclination (steepness) of the cone resulted in the surface-parallel stress being tensional at the apex of the edifice but compressive in its periphery (see Figs. 8, 9). The latter influenced the orientation of concentric reverse faults on the flanks, which became shallower with increasing flank inclination near the surface. The region of apical extension increases and the subsiding area was larger, compared with plateau-shaped experiments (Fig. 2). In dry sand experiments, flank oversteepening of the initial steep cones (>20°) produced grain-flow processes and occasionally outward-directed slides.

Pure evacuation collapse

In pure evacuation experiments, a balloon was inflated prior to its emplacement at the desired depth. The reservoir was then evacuated, simulating chamber deflation by, for example, magma withdrawal from a magma chamber, causing the chamber roof to subside. On evac-

Table 1 Selected experiments and measured geometric structures, for 16-cm balloon diameter. Column 1 is the model description and identifies the experiment (e.g. Exp5) and the cycle of resurgence (Zykl1–3). *F* Experiments in flour, *S* sand; if not specified each experiment was modelled twice using both materials average values. Columns 2–11 present the measured maximal distribution of structures. Column 12 summarises types of subsidence (*HS* horseshoe shaped; *BL* bench-like; *P* piston; *PM* piecemeal). *n.d.* Not defined

Model description	Chamber depth	Initial slope inclination, 0=plateau	Steepness after doming	Radial cracks diameter	Apical graben diameter	Subsidence apical graben	Concentric peripheral fault diameter	Concentric peripheral fault length	Ring fault diameter	Subsidence ring fault	Remarks
	(cm)	(°)	(°)	(cm)	(cm)	(cm)	(cm)	(°)	(cm)	(cm)	
Doming and evacuation experiments with two cycles of resurgence and withdrawal											
Exp12Zykl1	5	0	28	20	7	0.5	22	20	18	0.6	HS PM
Exp12Zykl2	5	0	36	27	9	1	28	9	18	1.3	HS PM
Exp12Zykl3	5	0	30	30	11	1.5	28	3	19	2	PM
Exp13Zykl1	5	10	30	23	6	0.3	23	12	18	0.3+0.3	HS PM
Exp13Zykl2	5	10	30	26	8	1.4	24	8	19	1HS+0.3	PM
Exp13Zykl3	5	10	35	28	10	1.5	24	7	19	2	PM
Exp14Zykl1	5	20	35–40	20	7	1.5	22	10	18	0.8	PM
Exp14Zykl2	5	20	40	24	11	1.5	24	6	19	1.8	PM
Exp14Zykl3	5	20	40	25	ca.12	1.5–2	24	3	19.5	2.3	PM
Exp15Zykl1	5	30	44	19	8	1.2	20.5	7	16	0.3	HS PM
Exp15Zykl2	5	30	45	20	10	1.5	21	6	17	0.3	PM
Exp15Zykl3	5	30	48	23	13	1.8	23	5	17	0.6	PM
Exp4Zykl1	7	10	30	22	7	0.5	24	15	17	0.5	HS
Exp4Zykl2	7	10	35	23	8	1	25	8	18	1	PM
Exp4Zykl3	7	10	40	26	n.d.	n.d.	27	5	20	1.2	PM
Exp5Zykl1	7	0	20	20	5	0.5	22	15	16	0.3	HS
Exp5Zykl2	7	0	30	26	7	1	24	5	17/19	0.7	PM
Exp5Zykl3	7	0	30	28	9	2	27	4	17.5	2	PM
Exp16Zykl1	9	0	27	21	7	1.8	22.5	19	14	0.6	Fig. 7
Exp16Zykl2	9	0	28	25	12	1.5	27	10	16	1.8	PM
Exp16Zykl3	9	0	28	30	15	1	29	6	20	2	PM
Exp17Zykl1	9	5	28	20.8	6.5	1.6	22	16	14.6	0.7	Fig. 7
Exp18Zykl1	9	10	30	19.8	6	2	23	14	14.6	0.5	Fig. 7
Exp19Zykl1	9	15	34	19.5	7.5	1.8	21	10	14.8	0.6	Fig. 7
Exp19Zykl2	9	15	35	22	9	1.3	25	7	15.5	0.9	PM
Exp19Zykl3	9	15	33	28	10	1	29	6	17.3	1.3	PM
Exp20Zykl1	9	20	35	19.5	7	2.2	20.5	9	15.3	0.6	Fig. 7
Exp21Zykl1	9	25	39	19.3	7.5	1.9	20.3	8.5	15.6	0.7	Fig. 7
Exp22Zykl1	9	30	44	18.5	8	2	20	7	16	0.6	Fig. 7
Exp22Zykl2	9	30	50	27	9	2.3	29	9	21	0.7	PM
Exp22Zykl3	9	30	37	30	12	2.5	29	6	22	1.2	PM
Exp2Zykl1	11	30	40	33	7	n.d.	34	8	17	0.8	
Exp2Zykl2	11	30	45	35	n.d.	n.d.	34	8	21	2.2	PM
Exp2Zykl3	11	30	50	34	n.d.	n.d.	34	8	23	2.5	PM
Exp1Zykl1	11.5	35	40	30	n.d.	n.d.	18	12	17	1.5	HS
Exp1Zykl2	11.5	35	60	36	n.d.	n.d.	29	5	21	4	PM
Exp1Zykl3	11.5	35	60	36	n.d.	n.d.	33	5	25	4	PM
Pure evacuation experiments											
[F] Exp23	5	0	n.d.	n.d.	n.d.	n.d.	24.3	n.d.	17.4	0.4	Fig. 4
[S] Exp24	5	0	n.d.	n.d.	n.d.	n.d.	22	n.d.	19	2	BL
[F] Exp27	7	0	n.d.	n.d.	n.d.	n.d.	23	n.d.	17.2	0.4	Fig. 4
[S] Exp28	7	0	n.d.	n.d.	n.d.	n.d.	22	n.d.	16.5	0.7	BL
[F] Exp30	9	0	n.d.	n.d.	n.d.	n.d.	20.5	n.d.	14	0.6	Fig. 4
[S] Exp31	9	0	n.d.	n.d.	n.d.	n.d.	20	n.d.	14	0.9	BL
[S] Exp33	11	0	n.d.	n.d.	n.d.	n.d.	18.5	n.d.	13	1	BL
[F] Exp34	11	0	n.d.	n.d.	n.d.	n.d.	17.8	n.d.	13.7	0.7	Fig. 4
[F] Exp36	13	0	n.d.	n.d.	n.d.	n.d.	14.5	n.d.	12.5	0.7	Fig. 4
[S] Exp37	13	0	n.d.	n.d.	n.d.	n.d.	15	n.d.	13.3	1.6+0.2	HS
[F] Exp38	15	0	n.d.	n.d.	n.d.	n.d.	12	n.d.	10	2	P
[S] Exp40	15	0	n.d.	n.d.	n.d.	n.d.	n.d.	n.d.	9.5	2	P

uation, slight downsagging (<0.5 cm) was the initial surface expression, followed by failure along numerous discrete sub-circular concentric fractures on the surface (Fig. 3). Modelling different heights of the plateau showed the third dimension of these faults to be mostly outward dipping (i.e. “bell-shaped”; Fig. 3), corroborating previous studies (e.g. Marti et al. 1994; Roche et al. 2000). This set of curved faults propagated from the reservoir upwards, where the first underground faults were arranged sub-horizontally above the centre of the balloon, followed by steeper synthetic faults (main ring faults; Fig. 3). At the surface, theseconcentric faults defined an en echelon pattern, forming a circular arrangement around a central collapse basin. Wedge-shaped and crescentic blocks slumped and tilted from the outer undisturbed wall into the basin along a set of interconnected antitheticlistric faults. Failure of hanging-wall blocks occurred, causing the caldera rim to propagate outwards (Fig. 3).

No radial cracks developed during the pure evacuation collapse experiments (cf. Marti et al. 1994). The central basin subsided largely as a piston but was repeatedly dissected to crescentic benches bound by two or three outward-dipping concentric faults reaching the surface (Fig. 3). This was more common in experiments with a shallow chamber (i.e. 5–8 cm). Some experiments developed a discrete circumferential zone of vertical to inward-dipping normal faults, with a total diameter larger than the simulated magma chamber, but lacking a significant dilation. As pointed out by Roche et al. (2000), these were triggered by outward-dipping reverse faults. Inward-tilted wedges formed that were defined by such antithetic periphery cracks and the outer ring fault(s) (Figs. 3, 4).

To evaluate the influence of the initial topography, the deflation experiments were performed beneath cones with an initial flank steepness of 10, 15, 20, 25 and 30°. With larger initial flank inclination, the central collapse basin was fractured in an increasingly chaotic manner. The position of concentric fractures was influenced by gravity load and gradually shifted outwards with increasing cone inclination. Increasing the chamber depth caused a systematic decrease of the near-surfacediameters of the encircling concentric faults (Fig. 4).

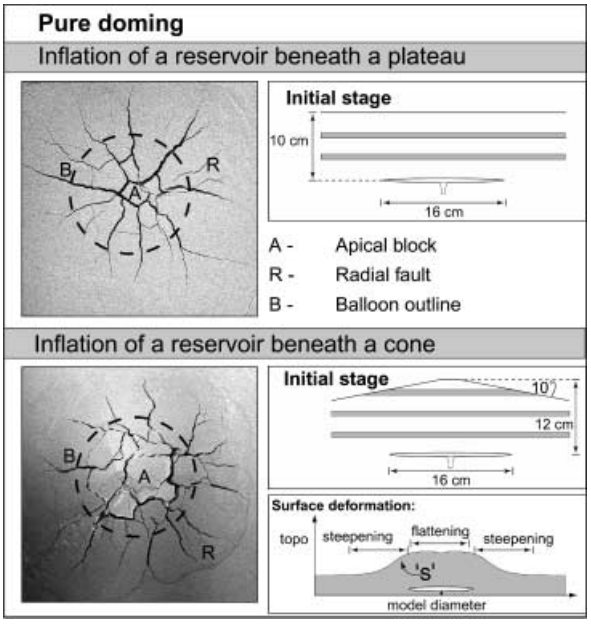

Fig. 2 Photographs of doming experiments in flour taken from the top and sketch of initial experimental conditions. *Inset lower right* outlines the regions of morphological steepening and flattening (not to scale)

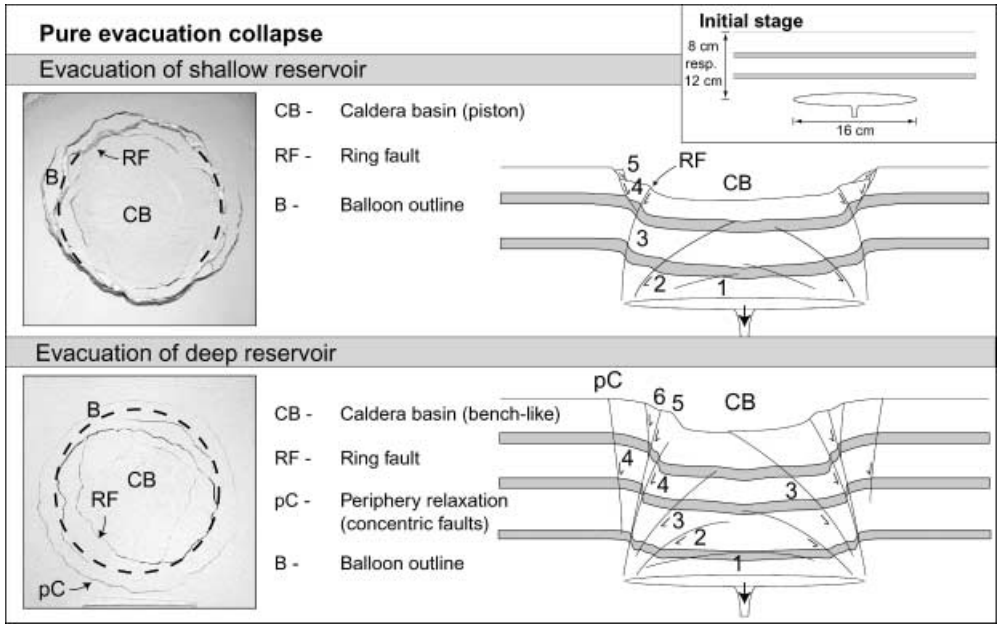

Fig. 3 Pure evacuation collapse of an analogue magma chamber beneath an initial plateau surface. Photographs of flour experiments and schematic profiles from sectioned experiments show the structural development of a shallow and a deep magma chamber. Separate experiments near a glass pane allowed assignment of numbers, indicating the chronological order of the faults

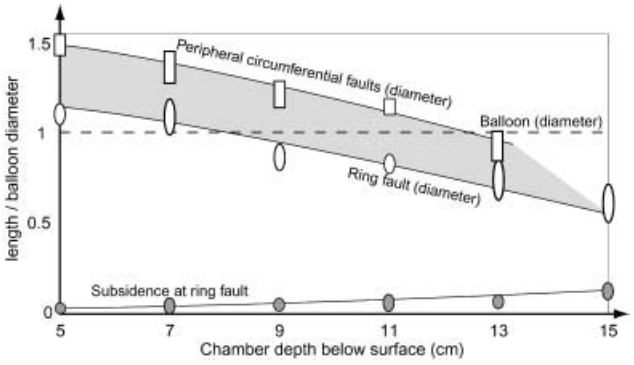

Fig. 4 Plot for pure evacuation experiments beneath a plateau showing chamber depth vs length of the measured structures (ring fault diameter, ring fault subsidence, diameter of periphery circumferential faults, balloon diameter) as a function of the balloon diameter. Data points at variance due to analogue materials are shown as vertically elongated and were connected by a "best-fit" curve. Increasing chamber depth shows a slight increase of the ring fault subsidence rate, a decrease of the diameter of the major ring faults and a decrease of the peripheral circumferential faults. One centimetre in experiments corresponds to approximately 1 km in nature

Doming and collapse

Experiments were designed to simulate doming and subsequent chamber evacuation, focusing on the interaction of the resulting structures. Doming reproduced the tumescent fault arrangement, i.e. radial cracks and subordinate concentric reverse faults,followed by encircling or horseshoe-shaped faults which define an apical graben with a mean diameter approximately half of the reservoir diameter (see Fig. 7).

Subsequent evacuation resulted in a closure of the radial cracks, accompanied by two concentric domains: (a) a bell-shaped fracture system forming the major caldera basin (main ring fault); and (b) periphery en echelon faults with diverse dips. The outermost concentric peripheral faults formed outside the extent of the visible radial doming cracks, whereas the inner concentric caldera faults crosscut them (Figs. 5, 6). The interaction of reversal reactivated radial fractures and newly formed concentric collapse faults generated a heterogeneous polygonal intracaldera structure and non-coherent caldera subsidence in all cyclic experiments.

The maximum cumulative caldera subsidence was a combination of apical graben fault displacement plus ring–fault subsidence. Surprisingly, in plateau experiments with equivalent volumes of inflation and subse-

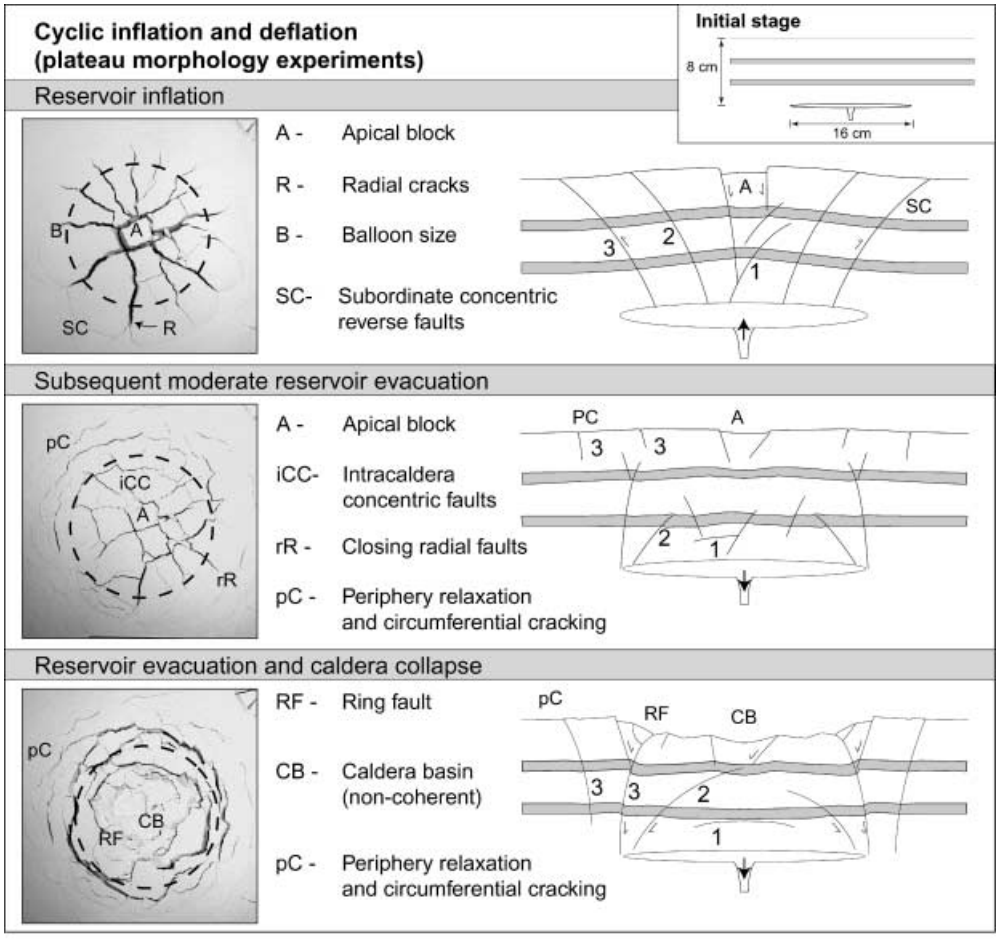

Fig. 5 Photographs and schematic profiles of experiments showing the structural development for chamber inflation and subsequent evacuation beneath a plateau (flour). The *numbers* indicate the chronological order of the faults

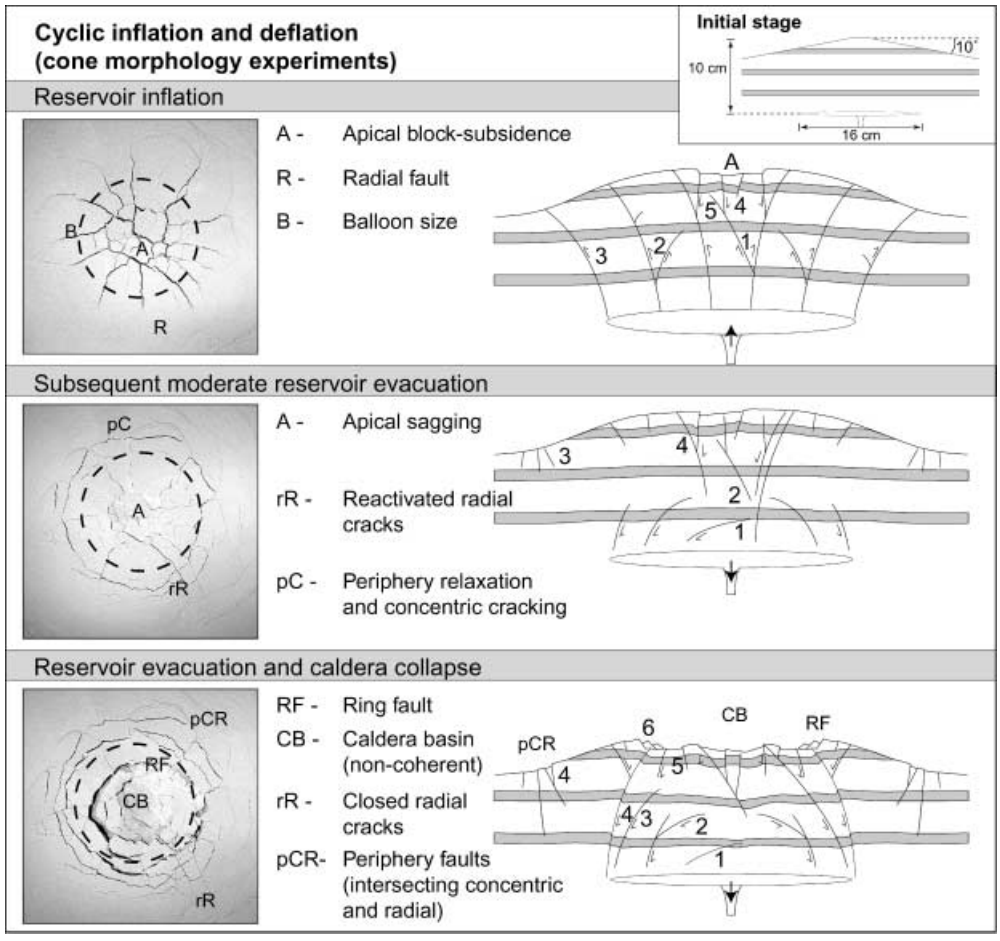

Fig. 6 Photographs and schematic profiles of experiments (flour) with initial cone morphology, showing the structural development for chamber inflation and subsequent evacuation. The *numbers* indicate the chronological order of the faults

quent deflation, the ratio of apical subsidence versus caldera subsidence was approximately 1 (Table 1). The diameter of the caldera ring-fault was ca. 1.5 times larger than the apical graben diameter for shallow chamber depths and largely unaffected by the cone geometry (Fig. 7). With increasing chamber depth, however, this discrepancy shrunk.

On evacuation, during initial sagging of the structural dome, synthetic and antithetic fractures formed wedges in the outermost periphery (Figs. 5, 6). These concentric peripheral fractures rooted at depths near the reservoir(s) but 2–5 cm beyond the horizontal extent of these (Fig. 8). Their surface expression caused terraces as well as horst and graben structures, 2–4 cm in length. Concentric peripheral faults were most common and dilation was strongest on cone-shaped edifices. The formation of these concentric peripheral faults, together with crosscutting radial faults requires a structural interplay of doming and evacuation collapse. Since tumescence influenced a greater area at the surface than the bell-shaped ring faults, this structural incongruity resulted in gravitational flank relaxation during chamber evacuation and the formation of circumferential peripheral fractures on the outer flanks of the edifice.

On second resurgence, many of the faults were reactivated: existing radial fractures reopened, and supplementary steepening of the flanks as well as a closure of the

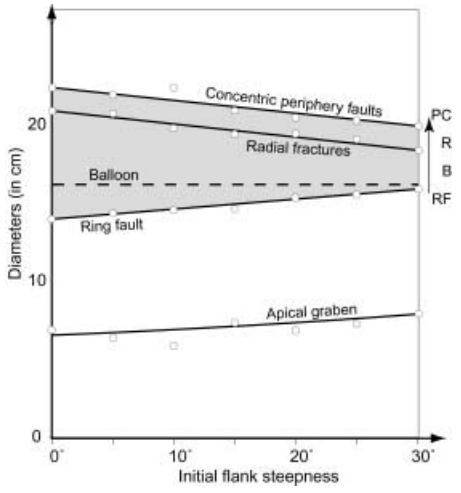

Fig. 7 Plot of multi-stage flour experiments of cone morphology: increasing initial inclination of the flanks of the cones (0, 10, 15, 20, 25, 30°) vs measured diameter. The initial topography slightly influences the diameter of radial cracks (*R*), the apical graben and the ring fault (*RF*) diameter. During subsequent balloon deflation, the diameter of concentric peripheral faults (*PC*) decreases with increasing initial flank steepness. "Best-fit" curves, where the shaded area includes the relations of *RF*, *B*, *R* and *PC*. The balloon (*B*) was situated at a depth of 9 cm below the surface; 1 cm in experiments corresponds to approximately 1 km in nature

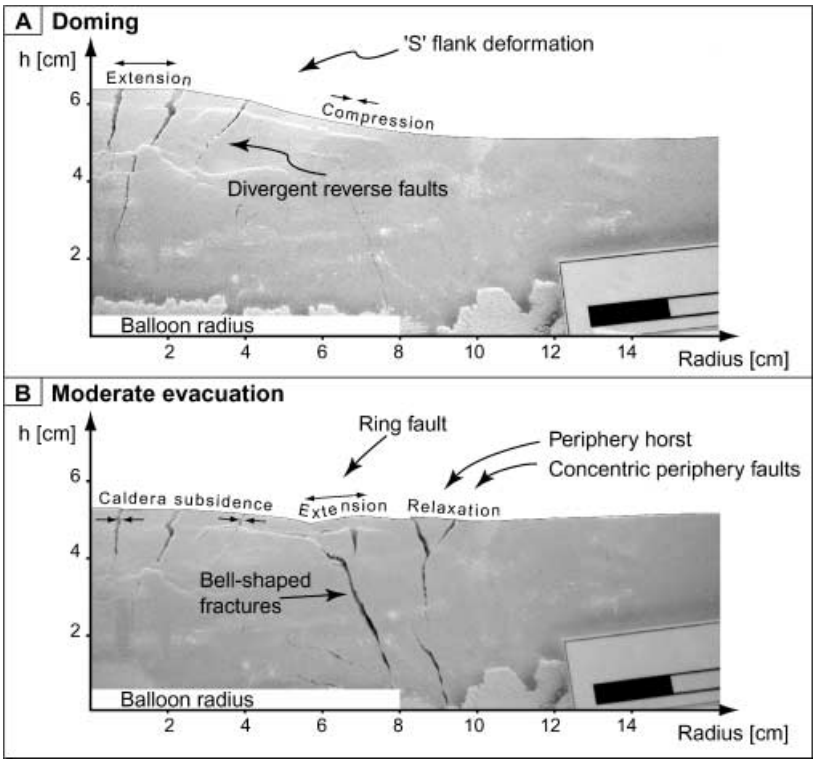

Fig. 8A, B Photographs of sections through the edifice illustrating doming and subsequent evacuation collapse. Deformation was simulated in flour adjacent to a pane of glass and photographed to record the fracture formation of **A** inflation causing tumescence and s-shaped flank deformation of an initial plateau surface, initiated by divergent reverse fractures. Note the flattening of the apical centre. **B** Subsequent deflation of ca. 50 % produces bell-shaped fractures and a contraction of the central material towards the shrinking magma reservoir, defining a caldera subsidence along a major ring fault. Relaxation of the flanks produced periphery faults and wedges, as well as horst and graben structures

peripheral faults occurred. The widespread slumps of the ring-fault hanging walls into the caldera basin resulted in an accumulation of wall material in the subsided central basin. With recurrently increasing volume of the balloon, outward-dipping ring faults and structures of the non-coherent caldera floor were reactivated so as to cause a space problem, resulting in additional fracturing. With each further cycle (a) radial domestructures propagated outwards and increased in quantity, and (b) reactivated concentric faults shifted outward, accompanied by outward-propagating flank steepening. During further cycles of doming and evacuation collapse, the outermost domed flanks remained as morphological highs (Fig. 8). Balloon resurgence in sand models formed supplementary faults to the fault patterns described above and incrementally destabilised the steepened and fractured flanks, which frequently collapsed and formed outward-directed slides. Such sliding sectors were bound and initiated by revived radial cracks and concentric peripheral faults. The occurrence and size of lateral failures is thought to be a function of the initial flank inclination, the quantity of radial fractures, and the position and depth of peripheral relaxation faults.

Summary and discussion

A variety of geometric models of caldera formation have been suggested, including the piston caldera (Anderson 1937; Williams 1941; Smith and Bailey 1968; Lipman 1997), the funnel-type caldera (Aramaki 1984; Yokoyama and Ohkawa 1986), the trap-door (Steven and Lipman 1976) and downsag caldera (Walker 1984), and the non-coherent or chaotic-type caldera (Scandone 1990; Branney and Kokelaar 1994; Mooreand Kokelaar 1998). In order to comprehend such complex caldera structures, simulation in analogue experiments was employed using the two end-member mechanisms of doming (Komuro 1987; Marti et al. 1994) and evacuation collapse (Roche et al. 2000), but also a combination of both mechanisms, i.e. the inflation and subsequent deflation of a reservoir.

Doming

During “dome-shaped” uplift, tensile stress is predominant at the centre of the dome, causing magma intrusion along normal faults, balanced by the overpressure of magma within the dyke. The propagation of dykes stops and they close when magma pressure has been reduced to a value equal to the stress across the dyke (McLeod and Tait 1999). Following the experimental observations, dykes are thought to propagate primarily in a radial mode during doming (Fig. 9A). A structural dome increases the edificevolume and results in steepening of the volcano flanks and a compressive stress regime in the caldera periphery. Extension is strongest in the apical region, resulting in subsidence of a graben. The experiments may provide an assessment of early apical subsidence in natural calderas, subsequently overprinted by ongoing caldera evolution (cf. Troll et al. 2000). Such apical graben subsidence, accomplished by slumping of large blocks into the expanding centre, may produce pressure jumps in the associated shallow magma reservoir and possibly trigger large-scale ash-flow eruptions (Gudmundsson 1998).

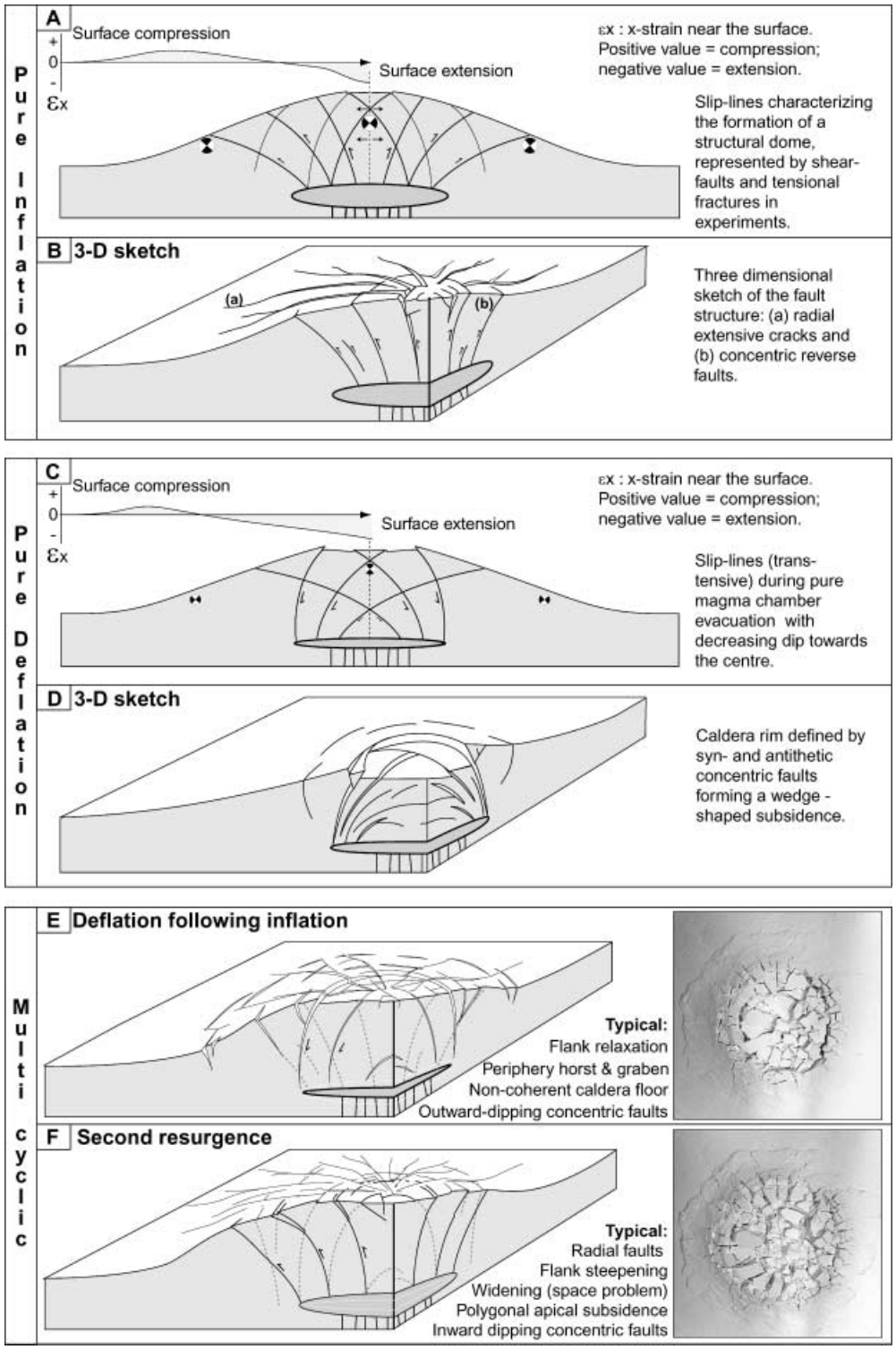

Fig. 9 Three-dimensional reconstruction of characteristic structures formed during **A, B** pure inflation, **C, D** pure deflation and **E, F** multi-stage inflation and subsequent deflation

Evacuation collapse

Reduction of the pressure inside the analogue magma chamber causes a gravity-driven downward displacement of the chamber roof into the reservoir (Fig. 9B). Major ring faults develop that are outward dipping with a curved outline (cf. Marti et al. 1994; Roche et al. 2000). With decreasing depth, the influence of maximum principal stress decreases so that the shear stress on the potential fault plane is sufficiently large to generate a shear fracture approaching this plane, leading to curved ring faults. In several experiments, subsidence was slightly delayed following balloon evacuation, suggesting that faults may remain active during and following magma chamber evacuation until their expression reaches the surface, implying a temporal hiatus within the edifice.

Combined doming and evacuation collapse

Initial reservoir inflation generates radial cracks and subordinate concentric reverse faults, causing flank deformation and an apical subsidence. Subsequent deflation of the reservoir generates caldera structures that overprint the previously domed edifice. When chamber evacuation is initiated, the area above the chamber sags, resulting in closure of the radial cracks. Subsequently, caldera ring faults and peripheral circumferential fractures form simultaneously. The location of the peripheral fractures may be several kilometres away from a caldera rim. As a consequence of the intersecting radial and concentric fault systems, the caldera floor fractures sequentially and subsides in a disjointed manner by reactivating radial structures and a set of newly formed bell-shaped faults. Erosion and inward slumping of megablocks is common, leading the caldera rim to propagate outwards (Lipman 1997; Roche et al. 2000). The structural network of intracaldera radial and concentric fractures is also present on the flanks of the edifice, where these form as a result of: (a) flank deformation and steepening; (b) radial fracture propagation during doming; and (c) circumferential faulting produced by flank relaxation upon chamber evacuation (Fig. 9). In this, three concentric fault domains are discriminated by the position, mechanism and chronology, i.e. the apical graben faults, the circumferential peripheral faults and the caldera ring faults. In caldera volcanoes with several stages of doming and evacuation, the extent of radial faults and the diameter of concentric faults is thought to migrate outwards with each additional stage. In this case, the number of faults increases incrementally (Table 1), reducing the stability of the volcano flanks. Whether doming precedes reservoir evacuation, or resurgent doming succeeds pure evacuation collapse, has no effect on the general structural arrangement.

Effect of initial edifice geometry

The state of stress within a multicyclic caldera volcano is strongly controlled by the magma chamber(s), but is also influenced by gravitational near-surface stresses due to pre-existing topography. The effect of topography is most pronounced for the distribution and location as well as the orientation of the concentric fracture systems. The dip-line curvature of reverse doming faults enhances with steeper initial volcano flanks. In turn, if the magma chamber evacuates beneath a steep cone, the concentric peripheral fractures have a less pronounced tendency to form open faults. Moreover, the central collapse basin fractures in a more disorganised way (Fig. 6). For irregular edifice morphologies, the caldera floor is likely to be piecemeal, even in pure evacuation experiments, since fractures arrange less uniformly compared with symmetric volcano-morphology experiments (Table 1). For cone morphologies not directly centred above the chamber, the pattern of radial fractures is uniform only near the centre. Away from the centre, the radial fractures propagate dominantly parallel to the dip line of the slope. Chamber evacuation beneath a slope produces concentric fractures with non-uniform fault offset, resulting in a tilted caldera floor.

The position of the chamber beneath the surface influences the geometric arrangement of the subsurface structures, confirming the emphasis placed on the roof aspect ratio by Roche et al. (2000). For shallow chambers, the distribution of concentric fractures reflects the chamber geometry. For larger chamber depths, however, this structural mirror becomes less pronounced.

Natural examples

The near-surface structural arrangements that result from magma chamber inflation, chamber evacuation, and repeated chamber withdrawal and replenishment stages, as seen in experiments, are recorded at several active and extinct volcanoes.

Tumescence

Examples of volcanic tumescence are provided by recent ground deformation measurements at, for example, Long Valley Caldera (Simons et al. 2000) and Campi Flegrei, Italy (Usai et al. 2000), illustrating amounts of resurgent doming of 2–4 cm year^{-1}, the latter example with a maximum annual uplift of ca. 40 cm year^{-1} in the early 1970s. The reconstruction of large-scale dome-shaped uplift induced by chamber inflation in the Aizu and Motojuku district of NW Japan showed circular shapes of 20–60 km in diameter, with amounts of domal uplift prior to caldera collapse of the order of 500–1000 m (Fujita et al. 1970; Komuro et al. 1984). In the Tertiary Rum Igneous Complex, Scotland, doming resulted in a tremendous basement uplift of approximately 1000–1500 m (Emeleus 1997; Troll et al. 2000). This wide range of recorded tumescence rates in natural volcanoes is well recorded in our doming experiments, where maximum uplift rates translate to several 100 m in nature.

The patterns of eruptive fissures on the Galapagos island volcanoes include radial fissures and dike swarms, and are thought to be related to dome-shaped uplift triggered by magmachamber inflation (McBirney and Williams 1969; Simkin and Howard 1970). On the island of Fernandina, doming caused annular dyking in the extensional apical region contemporaneous with radial dyke intrusion on the flanks of the volcano (Chadwick and Dieterich 1995; Rowland 1996). This is in agreement with the fracture arrangement observed in ourdoming experiments. This lateral and vertical expansion of the edifice causes “general expansion all around the volcano” (Walker 1999), putting the centre into tension, subsequently relived by normal fault caldera collapse (Gudmundsson et al. 1997).

Evacuation collapse

In turn, deflation of the magma chamber coupled with caldera collapse caused concentric faults to form at Darwin Caldera, Albemarle Island (McBirney and Williams 1969). An arcuate, flat-topped bench along the southern wall defines the caldera collapse basin, indicating that the engulfment of the caldera took place by at least two caldera ring faults forming two crescent plateaus. This compares well with the bench-like caldera floors observed in our pure evacuation set-ups.

The islands of Miyakejima and Sakurajima, Japan, are stratovolcanoes that erupted historically along radial fissures, thought to be associated with an expanding magma chamber (Ode 1957; Walker 1999). Numerous earthquakes have occurred beneath Miyakejima since 26 June 2000, with hypocentres initially beneath the island, moving westward (unpublished data of the Volcano Research Center, Earthquake Research Institute, University of Tokyo). Since 10 August 2000, intermittent phreatic eruptions have occurred on the summit, following roof collapse forming a small caldera 1.6 km across with a fault displacement of 450 m. The depression continued subsiding, accompanied by earthquake swarms and tilt changes. The amount of material erupted during the phreatic phase was <0.02 km^3 (before 10 August), contrasting with a subsidence volume of 0.45 km^3 inside the newly formed caldera. The cause of this was magma chamber deflation caused by drain back of magma that intruded laterally, implying that the eruption was induced by the collapse of the roof into an evacuated reservoir (Nakada and Fujii 2000). This also suggests that the process of caldera subsidence may be delayed by several weeks following evacuation, which compares well with the "time gap" observed in several of our experiments. Moreover, during subsidence of the Miyakejima caldera, concentricfaults formed crescentic terraces separating the caldera basin, whereas inward-falling crescentic megablocks widened the caldera rim and disguised the direct ring fault arrangement. Deflation in our experimental chamber caused an initial apical sagging and tilting of the flanks, until a delayed bench-like collapse of the caldera floor occurred. Tilting of the Miyakejima flanks displayed relaxation; however, the formation of peripheral fractures and horst and graben structures is, as yet, not well constrained.

Multi-stage caldera activity

Caldera resurgence that cause uplift of the caldera floor has been reported repeatedly, and several structural mechanisms including uplift of separate blocks, trapdoor uplift or coherent caldera floor uplift have been suggested in the literature (Lipman 1997). A space problem can arise when the resurgent block is structured by, for example, outward-dipping faults, as reported on Ischia caldera, Italy (Tibaldi and Vezzoli 1998). Our experiments show that bell-shaped outward-dipping faults are prone to become reactivated on resurgence, so that the caldera periphery is forced to uplift, and radial and concentric structures expand and dilate outwards. Similar mechanisms were suggested based on seismic data from Rabaul Caldera (Mori and McKee 1987; Jones and Stewart 1997).

On Gran Canaria (Canary Archipelago), caldera periphery faults and dyke-swarms surround the multi-stage Miocene Tejeda Caldera and are ordered in radial and concentric arrangement around the subaerial shield volcano (Schmincke 1967, 1968). At a distance of ~7 km from the ca. 20-km-wide central caldera, horst and graben structures are bound by radial faults and en-echelon-like concentric faults with normal and reverse sense. The latter are growth faults that formed during multicyclic ~20 ignimbrite eruptions (Schmincke 1994). The peripheral concentric and radial network of growth faults and dyke swarms reflects multi-cyclicity of the caldera that is consistent with the ignimbrite record and sheds light on mechanisms of "doming and collapse".

On OlympusMons, caldera periphery terraces are located at a distance of 50% of the volcano's radius from the caldera centre and are thought to be genetically related to magma chamber pulsation and the development of the large 100-km-wide central caldera basin (Thomas et al. 1990). On the edifice flanks, the position and explicitness of the peripheral terraces was controlled by chamber depth and initial morphology to form thrust faults, and genetically resembles the circumferential outer periphery belt produced in our multi-stage experiments.

Conclusion

The arrangement and distribution of peripheral caldera fractures is linked to the mechanism(s) by which calderas form. These mechanisms include the following:

1. Magma chamber inflation results in radial fractures and dyke injection, and an expansion of the flanks (doming; Fig. 9A, B). In the apical region, these structures are crosscut by chiefly concentric or horseshoe-shaped faults forming a polygonal apical graben (i.e. proto-caldera). Inward tilting and slumping of angular megablocks is common.
2. Pure evacuation collapse: Curved outward-dipping concentric faults encircle a collapsed caldera-basin including sharply defined ring faults (Figs. 9C, D). Additional characteristics are inward-slumped crescentic megablocks, growth faults plus the absence of widespread radial structures.
3. Multi-stage caldera volcanoes are recognised by a network of intersecting radial and concentric structures (dykes and faults) in the central caldera basin and the caldera's periphery (Fig. 9E, F). Moreover, peripheral relaxation during evacuation forms circumferential en echelon faults in normal and reverse sense and horst and graben structures in-between. These may be present several kilometres away from the caldera rim on the volcano flanks and could prompt major flank collapses.

The occurrence of peripheral circumferential faults crosscutting and crosscut by radial dykes or fractures requires at least one large incidence of doming or resurgence and one event of evacuation collapse. Based on the present experiments, a peripheral crosscutting radial and circumferential fault system suggests that caldera subsidence was necessarily non-coherent following a doming or resurgence event. This may illuminate the structural history of calderas that are covered by substantial caldera infill and/or where the intracaldera setting is obscured by later intrusions.

Acknowledgements The authors thank H.-U. Schmincke and M. Hort for discussions and critical reading of previous versions of the manuscript. We are grateful to R. Seyfried for remarks and N. Urbanski for assistance with experimental equipment. We thank P. Lipman and J. Stix for helpful comments, and A. Gudmundsson and O. Roche for stimulating reviews. Thanks go to VRC-ERI (Tokyo) for outstanding presentation of material related to the recent Mijakejima eruptions on the Web. Financial support was provided by the Deutsche Forschungsgemeinschaft (grants Schm 250/77–1 and Schm 250/72–1) to H.-U. Schmincke and a grant of the Studienstiftung des deutschen Volkes to VRT.

References

Anderson EM (1937) Cone sheets and ring dykes; the dynamical explanation. Bull Volcanol 1:35–40

Aramaki S (1984) Formation of the Aira caldera, southern Kyushu, ~22,000 years ago. J Geophys Res 89:8485–8501

Branney MJ (1995) Downsag and extension at calderas. New perspectives on collapse geometries from ice-melt, mining, and volcanic subsidence. Bull Volcanol 57:303–318

Branney MJ, Kokelaar P (1994) Rheomorphism and soft-state deformation of tuffs induced by volcanotectonic faulting at a piecemeal caldera, English Lake District. Bull Geol Soc Am 106:507–530

Byerlee J (1978) Friction of rocks. Pure Appl Geophys 116:615–626

Chadwick WW, Dieterich JH (1995) Mechanical modeling of circumferential and radial dyke intrusion on Galapagos volcanoes. J Volcanol Geotherm Res 66:37–52

Cobbold PR, Castro L (1999) Fluid pressure and effective stress in sandbox models. Tectonophysics 301:1–19

Druitt TH, Sparks RSJ (1984) On the formation of calderas during ignimbrite eruptions. Nature 310:679–681

Emeleus CH (1997) Geology of Rum and the adjacent islands. Mem British Geol Surv Scotland, Sheet 60

Fujita Y, Kawakita T, Arai T (1970) Tectonogenesis in the formative process of the Motojuku Green Tuff beds. Assoc Geol Collabor Japan 16:81–95

Glicken H, Janda RJ, Voight B (1980) Catastrophic landslide/ debris avalanche of May 18, 1980, Mount St. Helens volcano. EOS Trans Am Geophys Union 61:1135

Gudmundsson A (1988) Formation of collapse calderas. Geology 16:808–810

Gudmundsson A (1998) Formation and development of normal-fault calderas and the initiation of large explosive eruptions. Bull Volcanol 60:160–170

Gudmundsson A, Marti J, Turon E (1997) Stress fields generating ring faults in volcanoes. Geophys Res Lett 24:1559–1562

Hoshino K, Koide H, Inami K, Iwamura S, Mitsui S (1972) Mechanical properties of Japanese Tertiary sedimentary rocks under high confining pressures. Geol Surv Japan 244:1–200

Hubbert M (1937) Theory of scale models as applied to the study of geologic structures. Geol Soc Am Bull 48:1459–1520

Hubbert M (1951) Mechanical basis for certain familiar geologic structures. Geol Soc Am Bull 62:355–372

Jones RH, Stewart RC (1997) A method for determining significant structures in a cloud of earthquakes. J Geophys Res 102:8245–8254

Komuro H (1987) Experiments on cauldron formation: a polygonal cauldron and ring fractures. J Volcanol Geotherm Res 31:139–149

Komuro H, Fujita Y, Kodama K (1984) Numerical and experimental models on the formation mechanism of collapse basins during the Green Tuff orogenesis of Japan. Bull Volcanol 47:649–666

Krantz RW (1991) Normal fault geometry and fault reactivation in tectonic inversion experiments. Geol Soc Spec Publ 56:219–229

Lipman PW (1997) Subsidence of ash-flow calderas: relation to caldera size and chamber geometry. Bull Volcanol 59:198–218

Mandl G (1988) Mechanics of tectonic faulting; models and basic concepts. Elsevier, Amsterdam

Marti J, Ablay GJ, Redshaw LT, Sparks RSJ (1994) Experimental studies of collapse calderas. J Geol Soc London 151:919–929

Marti J, Folch A, Neri A, Macedonio G (2000) Pressure evolution during explosive caldera-forming eruptions. Earth Planet Sci Lett 175:275–287

McBirney AR, Williams H (1969) Geology and petrology of the Galapagos Islands. Geol Soc Am Mem 118:1–197

McLeod P, Tait S (1999) The growth of dykes from magma chambers. J Volcanol Geotherm Res 92: 231–246

Moore I, Kokelaar P (1998) Tectonically controlled piecemeal caldera collapse: a case study of Glen Coe volcano, Scotland. Geol Soc Am Bull 110:1448–1466

Mori J, McKee CO (1987) Outward-dipping ring-fault structure at Rabaul Caldera as shown by earthquake locations. Science 235:193–197

Nakada S, Fujii T (2000) Sequence and interpretation of Caldera-Forming Event at Miyakejima Volcano, Japan. EOS Trans Am Geophys Union 81:1258

Newhall C, Dzurisin D (1988) Historical unrest at large calderas of the world. US Geol Surv Bull 1855:1–1108

Ode H (1957) Mechanical analysis of the dyke pattern of the Spanish Peaks area, Colorado. Geol Soc Am Bull 68:567–576

Odonne F, Menard I, Massonnat GJ, Rolando JP (1999) Abnormal reverse faulting above a depleting reservoir. Geology 27:111–114

Prucha JJ (1965) Deformation of Silurian salt in Cayuga Rock Salt Company Mine, Myers, New York. EOS Trans Am Geophys Union 46:163

Ramberg H (1981) Deformation structures in theory and experiments. Geol Soc Sweden, 131 pp

Roche O, Druitt T, Merle O (2000) Experimental study of caldera formation. J Geophys Res 105:395–416

Rowland SK (1996) Slopes, lava flow volumes, and vent distributions on Volcano Fernandino, Galapagos Islands. J Geophys Res 101:23657–23672

Sanford A (1959) Analytical and experimental study of simple geological structures. Geol Soc Am Bull 42:19–52

Scandone R (1990) Chaotic collapse of calderas. J Volcanol Geotherm Res 42:285–302

Schmincke H-U (1967) Cone sheet swarm, resurgence of Tejeda Caldera, and the early geologic history of Gran Canaria. Bull Volcanol 31:153–162

Schmincke H-U (1968) Faulting versus erosion and the reconstruction of the mid-Miocene shield volcano of Gran Canaria. Geol Mitt 8:23–50

Schmincke H-U (1969) Ignimbrite sequence on Gran Canaria. Bull Volcanol 33:1199–1219

Schmincke H-U (1976) The geology of the Canary Islands. In: Kunkel G (ed) Ecology and biogeography of the Canary Islands. Junk, Holland, pp 76–184

Schmincke H-U (1994) Geological field guide of Gran Canaria. Part I and II. Pluto Press, Kiel, pp 1–64

Schultz RA (1996) Relative scale and the strength and deformability of rock masses. J Struct Geol 18:1139–1149

Simkin T, Howard KA (1970) Caldera collapse in the Galapagos Islands, 1968. Science 169:429–437

Simons M, Fialko Y, Rivera L, Chapin E, Hensley S, Rosen PA, Shaffer S, Webb FH, Langbein J (2000) Analysis of geodetic measurements of crustal deformation at Long Valley Caldera. EOS Trans Am Geophys Union 81:1322

Smith R, Bailey R (1968) Resurgent cauldrons. Geol Soc Am Mem 116:83–104

Steven TA, Lipman PW (1976) Calderas of the San Juan volcanic field, southwestern Colorado. US Geol Surv Prof Pap 958:1–35

Swanson DA (1982) Magma supply rate at Kilauea volcano 1952–1971. Science 175:169–170

Thomas PJ, Squyres SW, Carr MH (1990) Flank tectonics of Martian volcanoes. J Geophys Res 95:14345–14355

Tibaldi A, Vezzoli L (1998) The space problem of caldera resurgence: an example from Ischia Island, Italy. Geol Rundsch 87:53–66

Troll VR, Emeleus CH, Donaldson CH (2000) Caldera formation in the Rum Igneous Centre, Scotland. Bull Volcanol 62:301–317

Usai S, Sansosti E, Lanari R, Tesauro M, Fornaro G, Berardino P, Lundgren P (2000) Deformation time series analysis and modeling surface deformation observed with SAR interferometry at Campi Flegrei caldera. EOS Trans Am Geophys Union 81:1322

Walker GPL (1984) Downsag calderas, ring faults, caldera sizes, and incremental caldera growth. J Geophys Res 89:8407–8416

Walker GPL (1999) Volcanic rift zones and their intrusion swarms. J Volcanol Geotherm Res 94:21–34

Williams H (1941) Calderas and their origin. Univ Calif Berkeley Publ Geol Sci 25:239–346

Williams H, McBirney A (1979) Volcanology. Freeman, Cooper and Co., San Francisco

Wisser E (1927) Oxidation subsidence at Bisbee, Arizona. Econ Geol Bull 22:761–790

Ye S, Rihm R, Danobeitia J, Canales J, Gallart J (1999) A crustal transect through the northern and northeastern part of the volcanic edifice of Gran Canaria. J Geodyn 28:3–26

Yokoyama I, Ohkawa S (1986) Subsurface structure of Aira caldera and its vicinity in southern Kyushu, Japan. J Volcanol Geotherm Res 30:253–282